Materials Today 96 (2026) 103296

Contents lists available at ScienceDirect

Materials Today

journal homepage: www.elsevier.com/locate/mattod

Ultra-stable sodium-ion batteries enabled by single-atom tailoring of microbial hard carbons

Guilin Feng [a], Xiaohong Liu [b], Xiaoming Tu [c], Wen Xi [a], Hanying Wang [a], Lei Zhou [a], Chen Wu [d], Panpan Dong [a], Chunliu Xu [a], Weiqing Yang [a,*]

[a] Research Institute of Frontier Science and Key Laboratory of Advanced Technologies of Materials (Ministry of Education), School of Materials Science and Engineering, Southwest Jiaotong University, Chengdu 610031, China
[b] College of Materials and Chemistry & Chemical Engineering, Chengdu University of Technology, Chengdu 610059, China
[c] School of Integrated Circuit Science and Engineering (Exemplary School of Microelectronics), University of Electronic Science and Technology of China, Chengdu 6111731, China
[d] Natural Gas Research Institute of PetroChina Southwest Oil and Gas Field Company, Chengdu 610213, China

ARTICLE INFO

Keywords:
Hard carbons
Single-atom modification
Yeast-derived carbon
Cycling stability
Sodium-ion batteries

ABSTRACT

Hard carbons (HCs) are the most promising anodes for sodium-ion batteries, but their kinetics and cycling stability remain unsatisfactory. Herein, we introduce a universal strategy for decorating HCs with transition metal single atoms (SAs) using yeast cells as a sustainable biosorbent and template. The yeast's inherent negatively-charged functional groups and N/P-rich composition effectively coordinate and control the dispersion of metal ions, leading to the formation of stable SAs during pyrolysis. The optimized Cu-SA-modified HCs (YHCs-Cu SAs) achieves a high initial Coulombic efficiency of 86.7% and exceptional cycling stability, retaining 95% capacity after 2,500 cycles at 1C and demonstrating ultra-stable performance at 5C for 10,000 cycles (0.002% decay per cycle). Density functional theory calculations confirm that the Cu SAs reduce the Na^+ diffusion barrier, and in-situ Raman spectroscopy verifies Na^+ insertion into the graphitic domains during the low-voltage plateau. Notably, when extended to other transition metals (Fe, Ni, Co, Mn, and Zn), all YHCs-SA samples exhibit high-capacity retentions (>96% for around 120 cycles), significantly outperforming unmodified YHCs. This work establishes a novel biomass-based pathway for constructing single-atom-modified carbon materials, advancing the development of high-performance sodium-ion batteries.

Introduction

Sodium-ion batteries (SIBs) have emerged as a promising alternative to lithium-ion batteries for next-generation energy storage systems, owing to the natural abundance of sodium resources, similar working mechanisms, and favorable electrochemical charge–discharge properties [1–3]. Among various anode materials, hard carbons (HCs) have attracted considerable attention due to their abundant sources, tunable interlayer spacing, and rich nanopores and defects, which are conducive to sodium storage [4,5]. However, the widespread application of HCs is hampered by challenges such as low initial Coulombic efficiency (ICE) and unsatisfactory cycling stability [6,7]. To date, substantial research efforts have been dedicated to overcoming these limitations. Strategies include expanding the graphitic interlayer distance to facilitate Na^+ (de) intercalation, optimizing the porous structure to enhance Na^+ and Na cluster storage, introducing heteroatoms (e.g., N [8], P [9], F [10], O [11]) to modify the electronic structure, and engineering electrolytes to improve Na^+ desolvation and stabilize the solid-electrolyte interphase (SEI). While these methods effectively accelerate the development of HCs, there remains a need for more advanced approaches to precisely control the HC structure and interface.

Recently, the incorporation of transition metal single atoms (SAs) into carbon matrices has shown great promise for boosting the performance of HCs [12,13]. This strategy leverages the high atomic utilization efficiency and unique catalytic properties of SAs to enhance ICE and cycling stability. For instance, Zhao *et al.* synthesized Zn SAs in HCs, achieving an ICE of 84% and retaining 77% capacity after 5000 cycles at 2 A g^{-1} [14]. Similarly, Wang *et al.* and Cao *et al.* demonstrated the benefits of Ni [15] and Co [16] SAs, respectively, in delivering high specific capacity and exceptional long-term cyclability, primarily

* Corresponding author.
E-mail address: wqyang@swjtu.edu.cn (W. Yang).

https://doi.org/10.1016/j.mattod.2026.103296
Received 9 February 2026; Received in revised form 9 March 2026; Accepted 18 March 2026
Available online 31 March 2026
1369-7021/© 2026 Published by Elsevier Ltd.

attributed to the formation of a more stable SEI. Despite these advances, current synthesis methods often require extra N/P sources, which could lead to metal aggregation into clusters rather than isolated atoms. Furthermore, these complex synthesis methods, typically based on small-molecule precursors, are not readily applicable to sustainable, biomass-derived HCs.

In this study, we present a simple and scalable strategy for constructing transition metal SAs within biomass-derived HCs using live yeast as a biotemplate. Yeast cells naturally adsorb metal ions from solution via their negatively charged surface groups (–OH, –COOH etc.). During subsequent high-temperature pyrolysis, the intrinsically abundant N and P within the yeast biomass effectively anchor and stabilize the adsorbed metal ions as isolated single atoms, eliminating the need for external N/P heteroatom sources. The resulting optimized yeast-derived hard carbon with Cu single atoms (YHCs-Cu SAs) features suitable graphitic domains, highly developed nanopores (~1.2 nm), and a reduced defect content, collectively enabling fast Na^+ storage kinetics. The YHCs-Cu SAs anode delivers a high ICE of 86.7% and outstanding cycling stability, retaining 95.3% of its capacity after 2500 cycles at 1C and exhibiting a minimal decay rate of 0.002% per cycle over 10,000 cycles at 5C. Density functional theory (DFT) calculations corroborate a lower Na^+ diffusion barrier in the modified material, compared to pristine YHCs. XPS and TEM analyses confirm the formation of a thin and stable SEI on YHCs-Cu SAs, directly implicating the SAs in regulating SEI composition. Moreover, XRD, in-situ Raman, and GITT studies reveal a "adsorption-insertion-pore" filling sodium storage mechanism. This methodology is generalizable, as demonstrated with other transition metals (Fe, Ni, Co, Mn, Zn), all of which yield YHCs-SA samples with high capacity retention (>96% after ~120 cycles), significantly outperforming unmodified YHCs. The practical viability of our anode is further confirmed through robust performance in both half-cells at −20 °C and a full-cell configuration (YHCs-Cu SAs//NVOPF), which delivers a high energy density of 323 Wh kg^{-1}. In summary, our work establishes a novel and versatile biomass-based pathway for constructing single-atom-modified carbon materials. This strategy effectively regulates the SEI composition and enhances cycling stability, providing a viable and sustainable route for developing high-performance anodes for ultrastable SIBs.

Results and discussion

Construction of SAs in YHCs

Fig. 1a illustrates the synthesis of yeast-derived hard carbons (YHCs) modified with transition metal SAs. In a typical process, live yeast cells were cultured in a solution containing Cu ions (Cu^{2+}). The negatively charged yeast cell walls facilitated the efficient adsorption of Cu^{2+}. The resulting Cu-adsorbed yeast was then pyrolyzed at 1300 °C under an argon atmosphere to form the final YHCs. By precisely optimizing the Cu^{2+} concentration, YHCs embedded with copper single atoms (SAs) could be achieved. This is a distinct strategy that leverages the biomass's intrinsic composition. Morphological characterization by scanning electron microscopy (SEM) and transmission electron microscopy (TEM) reveals that the YHCs-Cu materials maintain a microsphere morphology (Figs. 1b, S1 and S2), indicating that Cu incorporation does not alter the overall structure inherited from the yeast template. Energy-dispersive X-ray spectroscopy (EDS) mapping confirms the homogeneous distribution of Cu throughout the carbon matrix (right of Fig. 1b). Furthermore, EDS

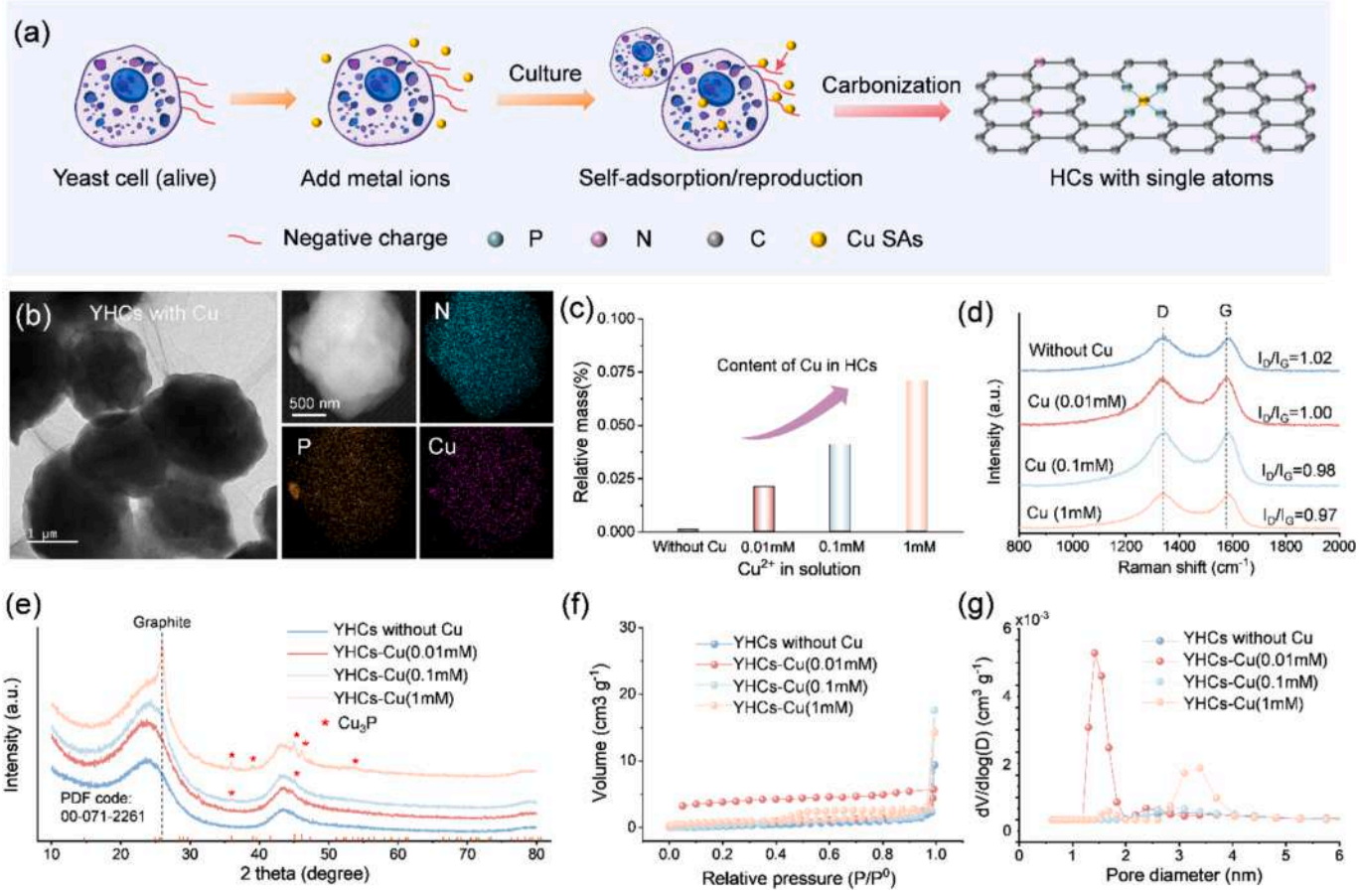


Fig. 1. (a) The preparation process of YHCs with single atoms; (b) TEM images of YHCs with Cu and corresponding Eds-mapping; (c) content of Cu in HCs as function of Cu^{2+} concentration in solution; (d) Raman results; (e) XRD results; (f) N_2 adsorption–desorption of the four samples; (g) corresponded pore distribution.

analysis (Fig. S3) shows that the levels of inherent heteroatoms (N, P) remain stable across all samples. In contrast, Fig. 1c shows that the Cu content in the final YHCs increases proportionally with the precursor solution concentration, verifying effective ion uptake by the yeast during culture. The structural evolution of the carbons was probed by Fourier-transform infrared (FTIR) spectroscopy, Raman spectroscopy, X-ray diffraction (XRD), and X-ray Photoelectron Spectroscopy (XPS). FTIR spectra (Fig. S4) show consistent C=C and O–H vibrations across all samples, confirming that Cu addition does not drastically alter the surface functional groups. However, Raman spectra (Fig. 1d) reveal a decrease in the I_D/I_G ratio with increasing Cu concentration, indicating a reduction in defect density and enhanced graphitization, likely catalyzed by Cu. This catalytic effect is further corroborated by XRD analysis (Figs. 1e, S5). While all samples display a broad (002) peak characteristic of disordered carbon, the sample with the highest Cu content (YHCs-Cu(1 mM)) exhibits a sharp graphite peak. The enhanced graphitic character is further confirmed by XPS C*1s* spectra (Fig. S6), where the highest-Cu sample shows a greater proportion of sp^2 carbon. Notably, distinct Cu_3P nanoparticle peaks emerge in the XRD patterns of YHCs-Cu(0.1 mM) and YHCs-Cu(1 mM), suggesting that excess Cu leads to nanoparticle/cluster formation, whereas lower concentrations favor the stabilization of SAs. Porosity was analyzed using N_2 adsorption–desorption measurements (Fig. 1f). The isotherms are Type IV, signifying the presence of micro- and mesopores. Crucially, pore size distribution analysis shows that YHCs-Cu(0.01 mM) possesses a significantly larger volume of micropores (1.0–2.0 nm) and a correspondingly higher micropore surface area (8.34 $m^2\ g^{-1}$) compared to other samples (<3.00 $m^2\ g^{-1}$). This demonstrates that a low, optimized Cu content effectively promotes the development of abundant micropores, which could be attributed to the reaction between partial Cu species and around carbon during carbonization, inhibiting the stacking of carbon layers. This is considered to favor the sodium storage in the electrochemical test.

We further examined the micro-morphology of the various YHCs via high-resolution transmission electron microscopy (HRTEM). A difference was observed at high magnifications in HRTEM images, revealing structural changes between the YHCs samples (Figs. 2a and b, S7). The microstructures, typically formed by a combination of localized graphitized regions and amorphous carbon domains, show that YHCs with high Cu exhibits a higher short-range order. Additionally, a reduced graphitic spacing was observed with the increase of Cu content (Fig. S8), reflecting that more Cu can increase the degree of graphite, likely due to the catalytic property of Cu [17]. To confirm the formation of Cu SAs at YHCs-Cu (0.01 mM), we conducted inductively coupled plasma (ICP), high angle annular dark-field scanning transmission electron microscopy (HAADF-STEM), and XPS tests. The ICP result reveals that the content of Cu is approximately 0.07%, which is low to minimize the possibility of Cu cluster formation in YHCs-Cu (0.01 mM). To further confirm the chemical states of Cu and P in the YHCs anode, the XPS spectra of P *2p* and Cu *2p* were analyzed in detail. The P *2p* peak appears

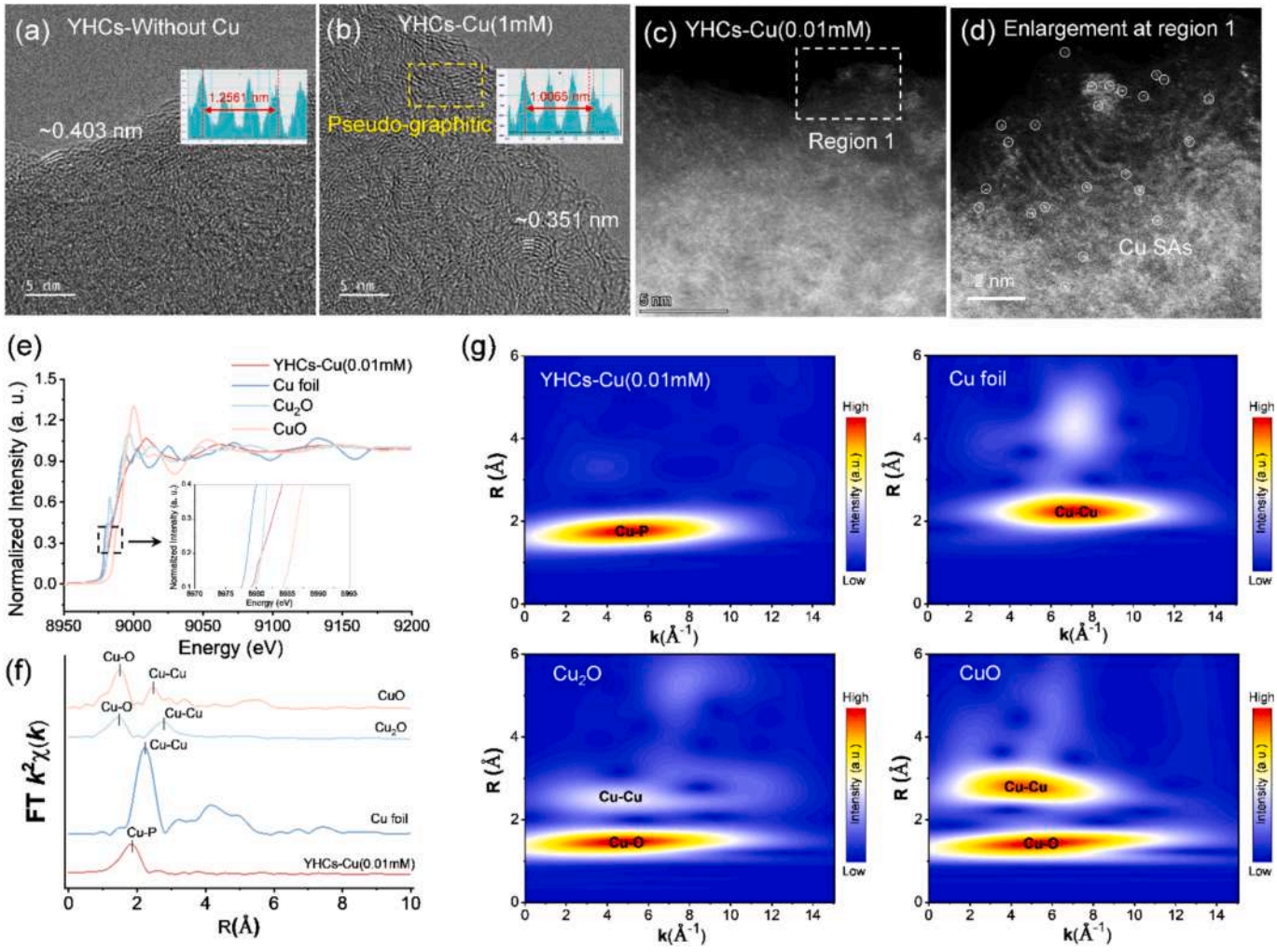


Fig. 2. HRTEM images of (a) YHCs without Cu and (b) YHCs-Cu(0.01 mM); (c) HAADF-STEM image of YHCs-Cu (0.01 mM); (d) enlargement at region 1 (white circles represent Cu SAs); (e) Cu K-edge XANES; (f) Fourier-transform EXAFS spectra; (g) Wavelet-transform of the k^2-weighted EXAFS data.

~130 eV, indicating the formation of Cu-P bonds in the Cu^{2+} adsorbed YHCs. Notably, compared with YHCs-Cu (1 mM), the main P *2p3/2* peak in YHCs-Cu (0.01 mM) shifts to a lower binding energy (Fig. S9). This phenomenon could be attributed to the formation of Cu–P–C structures in YHCs-Cu (0.01 mM), which modulates the electronic structure of the material. Additionally, the Cu *2p* analysis results are summarized in Fig. S10. With the decrease of Cu^{2+} concentration in YHCs, the Cu *2p3/2* peak shifts to a higher binding energy, suggesting the transformation of Cu^0 to $Cu^{\delta+}$. This is likely associated with the formation of Cu-P-C structures in YHCs-Cu(0.01 mM). As displayed in Figs. 2c, d and S11, there are numerous bright spots (marked by white circles) in the HAADF-STEM image, which indicates that Cu species are atomically dispersed in YHCs-Cu(0.01 mM). We further confirm the distribution of Cu SAs in YHCs by the STEM-EDS mapping in Fig. S12. The normalized Cu K-edge X-ray absorption near-edge structure (XANES) spectrum of YHCs-Cu(0.01 mM) is shown in Fig. 2e. The Cu K-edge lies between the Cu (Cu^0) and CuO (Cu^2) standard spectra, suggesting that the valence of Cu species is $0 < x < 2$.[18] Furthermore, the coordination environment of Cu species was investigated using the extended X-ray absorption fine structure (EXAFS). As shown in Fig. 2f, the dominant peak of YHCs-Cu (0.01 mM) is at ~1.8 Å, which is lower than the Cu-Cu pair (~2.2 Å) of Cu foil and higher than the Cu–O interaction (~1.4 Å) of CuO/Cu_2O. The EXAFS wavelet transform (WT) was adopted to further discuss the EXAFS oscillations of YHCs-Cu(0.01 mM). From the WT contour plots in Fig. 2g, there is only one peak at ~5.1 Å in YHCs-Cu(0.01 mM), which is different from those in Cu foil (~7.2 Å), Cu_2O (~5.5 Å) and CuO (~4.7 Å). The results of EXAFS mean that Cu species exist as SAs in the carbon frameworks and do not coordinate with O.[19] Moreover, the EXAFS curves of YHCs samples are fitted to accurately analyze the coordination environment of Cu, which suggests a Cu-P coordination in YHCs-Cu (0.01 mM) (Tab. S1, Fig. S13). All the results demonstrate that the existence of Cu SAs in YHCs-Cu(0.01 mM).

Electrochemical performance of different YHCs samples

To evaluate the Na^+ storage behavior of the prepared YHCs samples, we assembled half-coin cells and analyzed their electrochemical performance. Fig. 3a displays the initial charge/discharge profiles. The YHCs-Cu(0.01 mM) sample achieved the highest ICE of 86.7%, compared to 78.3% for pristine YHCs, 83.1% for YHCs-Cu(0.1 mM), and 81.3% for YHCs-Cu(1 mM). This indicates minimal sodium loss during the first cycle for YHCs-Cu(0.01 mM), which we attribute to the presence of Cu SAs modulating the composition of the SEI and reducing irreversible Na^+ consumption. Furthermore, the low-voltage plateau capacity, summarized in Fig. 3b, was significantly enhanced in the YHCs-Cu(0.01 mM) sample. This suggests that the optimized micropore structure contributes to superior Na^+ storage in the plateau region. The rate capability of the materials was tested across current densities from 0.1 to 10C (Fig. 3c). Compared with other three samples, YHCs-Cu(0.01 mM) consistently delivered the highest capacities. A summary of capacity retention at various rates is provided in Fig. 3d and YHCs-Cu (0.01 mM) shows a best capacity retention at high current density. These results demonstrate good kinetics in YHCs-Cu(0.01 mM), owing to the generation of Cu-P-C configuration enhancing Na^+ transportation. The long-term cycling stability was assessed at a rate of 1C (Fig. 3e, Fig. S14-S15). The YHCs-Cu(0.01 mM) electrode exhibited not only a high specific capacity but also exceptional retention, maintaining 95% of its initial capacity after 2,500 cycles, significantly outperforming the other samples. A more detailed analysis of the capacity retention at the 200th, 500th, and 1000th cycles (Fig. 3f) confirms that the incorporation of Cu SAs enhances cycle stability, with the YHCs-Cu(0.01 mM) sample showing the most excellent performance. This is likely due to the critical

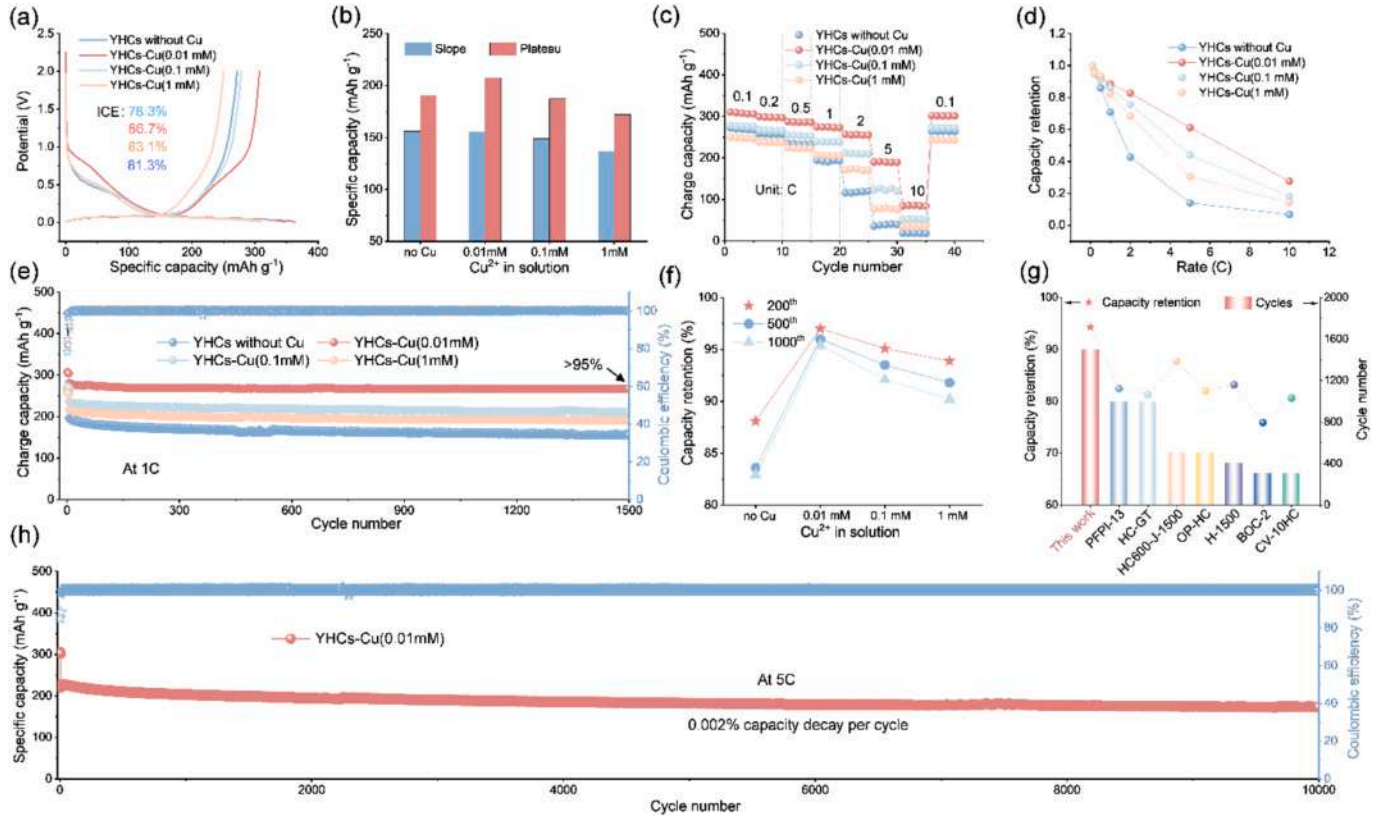


Fig. 3. (a) Discharge-charge curves of first cycle; (b) summarized slope and plateau capacity for the samples; (c) rate performance, and (d) capacity retention at various rates (1C = 300 mA g^{-1}, measured in 25 °C); (e) cycle performance at 1C; (f) capacity retention of the four samples at different cycles; (g) comparison of electrochemical performance at various current densities with HCs reported previously for SIBs: PFPI-13 [4], HC-GT [22], HC600-J-1500 [23], OP-HC [24], H-1500 [25], BOC-2 [26], CV-10HC [27]; (h) long cycle of YHCs-Cu(0.01 mM) at 5C.

role of Cu SAs in forming a more stable and ion conductive SEI. The impact of SA concentration was probed using a sample with lower Cu content (YHCs-Cu(0.001 mM)), which is expected to contain fewer Cu SAs. After ~900 cycles, this sample retained 96.1% of its capacity (Fig. S16), further corroborating the critical role of Cu SAs in improving cycle life. The superiority of our optimized material is further highlighted by a direct comparison with previously reported HCs in both ether- and ester-based electrolytes (Fig. 3g). The YHCs-Cu(0.01 mM) sample exhibits superior capacity retention, emphasizing the advantage of the Cu SAs modification. To assess the high-rate stability, the YHCs-Cu (0.01 mM) anode was cycled at a high current density of 3C and 5C (Fig. 3h, Fig. S17, Tab. S2). It retained 90% of its capacity at 3C after 1,800 cycles and 80% after 10,000 cycles at 5C, equating to a minimal decay rate of 0.002% per cycle. At 5C, it delivered a remarkable specific capacity of 217mAh g^{-1}, which is substantially higher than that of the pristine YHCs. Once a stable SEI forms, the capacity remains nearly constant, confirming the robust and sustainable structure of the YHCs-Cu(0.01 mM) anode. This outstanding long-term cyclability underscores the critical role of Cu SAs in maintaining structural integrity and electrochemical performance under demanding conditions.

Additionally, to elucidate the reaction kinetics and Na^+ storage behavior, we performed cyclic voltammetry (CV) measurements at sweep rates ranging from 0.1 to 1.0 mV s^{-1} (Fig. S18). The storage mechanism was analyzed using the power-law relationship between peak current (i) and sweep rate (v):[20]

$$i = av^b \quad (1)$$

where a and b are empirical parameters related to reaction mechanism. A b-value distinguishes between surface-controlled ($b = 1.0$) and diffusion-limited ($b = 0.5$) processes.[21] For the YHCs-Cu(0.01 mM) anode, the calculated b-values for the cathodic (i_p) and anodic (i_s) peaks were 0.56 and 0.68, respectively. In contrast, the pristine YHCs yielded significantly lower values of 0.37 and 0.45. The intermediate b-values for the Cu-modified sample indicate a mixed storage mechanism, with diffusion-controlled behavior remaining dominant at lower potentials. The consistently higher b-values further suggest enhanced Na^+ reaction kinetics, which we attribute to the Cu single-atom structure facilitating more efficient ion migration.

The role of atomic Cu-doping for the Na storage behavior

To elucidate the mechanism behind the enhanced Na^+ storage in Cu SA doped HCs, we conducted density functional theory (DFT) calculations. The computed Na^+ diffusion barrier for the atomic Cu-doped model was significantly lower than those for both pristine hard carbon and a Cu cluster-doped model (Figs. 4a, b, S19-20), indicating that Cu-P-C configuration could regulate the electronic structure of HCs, markedly accelerating Na^+ transport. This theoretical prediction is directly corroborated by experimental electrochemical data. The voltage profiles at various rates (Fig. S21) show that the YHCs-Cu SA electrode exhibits a minimal voltage polarization of 0.026 V, substantially lower than the 0.064 V observed for the pristine YHCs. This reduced polarization confirms the enhanced Na^+ migration kinetics, rationalizing the superior

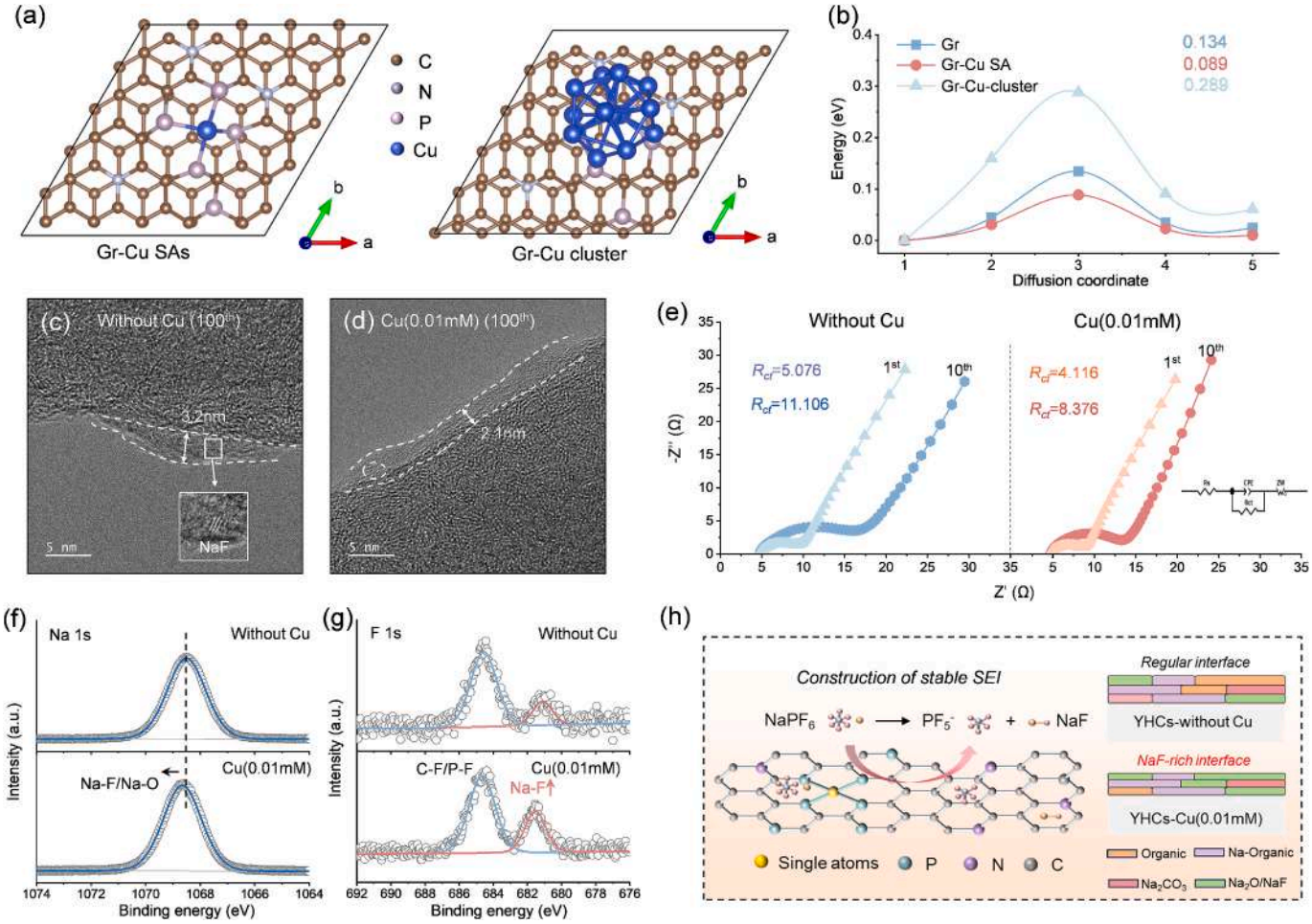


Fig. 4. (a) DFT calculations for Gr-Cu SAs and Gr-Cu cluster; (b) diffusion barrier energies of Na^+ in Gr, Gr-Cu SAs and Gr-Cu cluster; TEM images of YHCs after 100th cycles (c) without Cu; (d) Cu(0.01 mM); (e) EIS results; XPS spectra of the two samples after 100th cycles for (f) Na 1 s; (g) F 1 s; (h) schematic illustration of the structure of SEI layer of YHCs without Cu and YHCs-Cu(0.01 mM).

rate capability of the YHCs-Cu(0.01 mM) electrode. Given the critical role of the SEI in cycling stability, we systematically investigated the structure and composition of the SEI layers formed on the YHCs with and without atomic Cu-doping using HRTEM, EIS, and XPS. HRTEM analysis (Fig. 4c, d) identifies crystalline components within the SEI, with lattice fringes corresponding to the (1 1 1) planes of NaF and Na_2CO_3 (~0.25 nm).[28,29] Notably, the SEI on YHCs-Cu(0.01 mM) is thinner and more uniform than that on the undoped YHCs. We attribute this optimized morphology to the presence of Cu SAs, which promotes a more homogeneous and stable SEI formation. To further probe the interfacial kinetics, we performed electrochemical impedance spectroscopy (EIS). The Nyquist plots (Fig. 4e) were fitted with an equivalent circuit, revealing that YHCs-Cu(0.01 mM) exhibits a lower charge-transfer resistance (R_{ct}) and a reduced Warburg impedance (Z_w) compared to the undoped sample. This confirms that the Cu SAs enhance both the charge-transfer kinetics and the solid-state diffusion of Na^+, corroborating the kinetic advantages suggested by the DFT calculations. The chemical composition of the SEI was further analyzed by XPS. The deconvoluted Na *1s* spectra (Fig. 4f) show a peak for Na-O/Na-F species. A noticeable red-shift in the binding energy for YHCs-Cu(0.01 mM) suggests a difference in the chemical environment or composition of these species. To clarify this, we deconvoluted the F *1s* spectra (Fig. 4g), which revealed a higher NaF content in the SEI of the atomic Cu-doped sample [10]. This indicates that the Cu SAs actively regulate the decomposition of the electrolyte, favoring the formation of NaF. Additionally, the increased CO_3^{2-} content observed in the C *1s* spectra for the YHCs-Cu(0.01 mM) further confirms that Cu SAs regulate the chemical composition of the SEI (Fig. S22). Based on these combined findings, we propose a summarized function for Cu SAs in YHCs (Fig. 4h). The presence of atomic Cu catalysts promotes the preferential decomposition of the $NaPF_6$ electrolyte, leading to an increased generation of inorganics. This results in the formation of a dense, inorganics-rich interface. Such a stable SEI film effectively protects the carbon anode surface from continuous electrolyte breakdown, thereby significantly extending the cycling life of assembled SIBs.

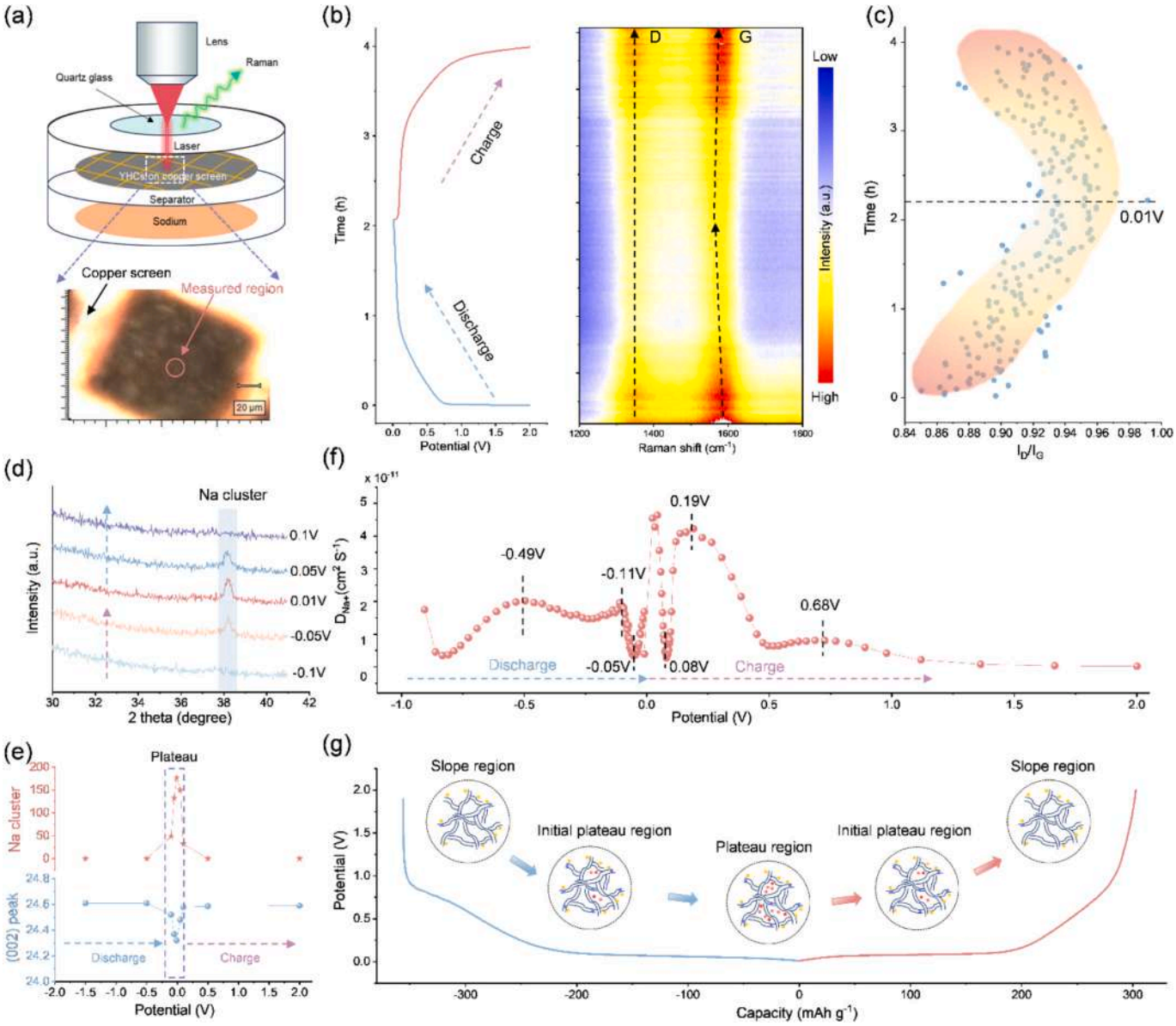


Fig. 5. (a) Profile of home-made *in-situ* Raman, copper screen as current collector; (b) Raman results during discharge–charge process; (c) summarized I_D/I_G as function of time; (d) XRD results at different discharge state; (e) conclusion of (002) peak and intensity of Na cluster during discharge–charge process; (f) GITT result of YHCs-Cu(0.01 mM); (g) proposed Na^+ storage mechanism.

Investigation on the storage mechanism of Na^+ in YHCs-Cu(0.01 mM)

To investigate the electrochemical reaction mechanism and structural evolution of the YHCs-Cu(0.01 mM) anode during the sodiation/desodiation process, we conducted a series of *in-situ* and *ex-situ* characterizations. Fig. 5a illustrates the self-assembled Raman cell, which utilized a copper mesh current collector and a quartz glass window to allow laser irradiation (532 nm) on the electrode surface and collection of Raman signal (Fig. S23). The Raman spectra, collected throughout the discharge/charge process (Fig. 5b, Fig. S24), reveal a reversible shift of the G band (~1588 cm^{-1}) to lower frequencies during discharge, particularly within the plateau region. This softening of the G band is indicative of Na^+ insertion into the graphitic layers, which weakens the C–C bonds by transferring electrons into the π* antibonding orbitals. In contrast, the D band (~1350 cm^{-1}) remains largely unchanged, suggesting that Na^+ adsorption at defect sites does not significantly alter the inherent defect structure [30]. The intensity ratio of the D to G bands (I_D/I_G) was further analyzed (Fig. 5c). This ratio increases during discharge, reaching a maximum at 0.01 V (fully discharged), and subsequently decreases upon charging. This trend indicates that the formation of quasi-metallic sodium clusters in the low-voltage plateau region introduces temporary disorder into the graphitic lattice [31]. Complementary *ex-situ* XRD analysis was conducted on electrodes at various states of discharge/charge, protected by a polyimide (PI) film to prevent air exposure (Fig. S25). After background subtraction, a prominent (0 0 2) diffraction peak is observed at ~24.2°. Notably, a new peak emerges at 38.2° at low voltages (0.05 V, 0.01 V, and −0.05 V), which we assign to quasi-metallic sodium (Fig. 5d), confirming Na cluster formation. The evolution of the (0 0 2) peak position and the intensity of the quasi-metallic Na peak are summarized in Fig. 5e. A slight downshift of the (0 0 2) peak upon deep discharge evidences the expansion of the interlayer spacing due to Na^+ intercalation, while the increasing intensity of the Na cluster peak correlates with deeper discharge states. To probe the Na^+ diffusion kinetics, we performed galvanostatic intermittent titration technique (GITT) measurements (Fig. 5f, Fig. S26). The calculated apparent Na^+ diffusion coefficient (D_{Na}^+) shows a fluctuation at ~−0.49 V, likely associated with SEI formation. Subsequent variations in D_{Na}^+ at ~−0.11 V correspond to Na^+ insertion processes. The decreasing trend of D_{Na}^+ from −0.11 to −0.05 V can be attributed to the extensive filling of Na^+ into the closed micropores of hard carbon, which increases ion transport resistance. In contrast, the rising D_{Na}^+ in the range of −0.05 to −0.01 V is associated with the formation of abundant quasi-metallic Na clusters within the micropores, suggesting a transition from the insertion-dominated to a pore-filling-dominated Na^+ storage mechanism [32]. The presence of sodium clusters was further verified through a phenolphthalein discoloration test (Fig. S27). YHCs-Cu(0.01 mM) Electrodes discharged to 0.1 V showed negligible color change, confirming that the capacity in the slope region originates from ionic adsorption. In contrast, electrodes discharged to 0.05 V and 0.01 V induced pronounced discoloration, providing visual evidence for the formation of quasi-metallic Na clusters. By integrating the findings from XRD, Raman, GITT, and the chemical test, we propose a three-stage "adsorption-insertion-pore filling" mechanism for Na^+ storage in YHCs-Cu(0.01 mM) (Fig. 5g, Supporting information): (1) Na^+ adsorption at surface/defect sites for slope region (high voltage); (2) Na^+ insertion into the graphitic interlayers (early plateau region); (3) Pore filling and the formation of quasi-metallic Na clusters within suitable nanopores (low-voltage plateau region).[33] This multi-modal storage mechanism synergistically contributes to the high capacity and excellent reversibility observed in our HCs anodes.

Application of YHCs SAs

To demonstrate the universal superiority of our strategy, we extended the synthesis to incorporate other transition metals, including Fe^{3+}, Ni^{2+}, Co^{2+}, Mn^{2+}, and Zn^{2+} into culture solution of yeast cells. After culturing and carbonization, the prepared samples were labeled as YHCs-Fe(0.01 mM), YHCs-Ni(0.01 mM), YHCs-Co(0.01 mM), YHCs-Mn (0.01 mM), and YHCs-Zn(0.01 mM), respectively. All these HCs present typical charge–discharge profiles in Fig. 6a. These transition metal SA-modified YHCs consistently demonstrate superior rate capability and cycling stability compared to the pristine sample (Fig. S28-29). This universal enhancement is quantified by their exceptional capacity retention, with all modified samples maintaining over 96% of their capacity during the first 100 cycle, a significant improvement over the unmodified YHCs (Fig. 6b). This robust performance across different metals strongly corroborates our findings for YHCs-Cu SAs and underscores the general role of transition metal SAs in stabilizing the electrode, primarily through the regulation of the SEI film. Further analysis of the voltage profiles reveals that all YHCs-SA samples exhibit reduced polarization in the low-voltage region compared to pristine YHCs (Fig. S30). This suggests that the SAs could facilitate the kinetics of sodium cluster decomposition or Na^+ desorption from the carbon interlayers. To assess practical applicability, we evaluated the electrochemical performance of YHCs-Cu(0.01 mM) at −20 °C, where it maintained considerable performance (Fig. S31). Furthermore, we assembled a full cell by pairing the YHCs-Cu(0.01 mM) anode with a $Na_3V_2O_2(PO_4)_2F$ (NVOPF) cathode, chosen for its high operating voltage (~4.3 V) and robust structure (schematic illustration of full cell was shown in Fig. 6c).[34] Ether-based electrolytes were employed to ensure stable high-voltage operation. The resulting NVOPF//YHCs-Cu(0.01 mM) full cell exhibits great rate performance across a wide range of current densities (0.1 to 5C, cathode-mass-based calculation) within a voltage window of 1.5–4.3 V (Fig. 6d and e). By integrating the capacity and voltage, we calculated an exceptional energy density of 435.6 Wh kg^{-1} at 0.1C (Fig. S32). We further compared our work with previously reported high-energy, high-power cathodes (Fig. 6f). These comparisons demonstrate that the NVOPF//YHCs-Cu(0.01 mM) system exhibits superior performance, confirming its suitability and potential for high-power applications. Impressively, the full cell also delivers good cycling stability, retaining 85.1% of its capacity at 3C (Fig. 6g). The operational state of a prepared full cell is shown in Fig. 6h. Collectively, these results compellingly highlight the potential of YHCs-Cu(0.01 mM) as a high-performance anode for practical SIBs.

Conclusion

In summary, we have developed a microbial strategy to synthesize Cu single-atom-tailored hard carbons (YHCs-Cu SAs) using yeast cells as a sustainable biosorbent and biotemplate. This method leverages the negatively charged surface functional groups (–OH, –COOH, etc.) of yeast to naturally adsorb metal ions from solution, while the intrinsic nitrogen and phosphorus species within the yeast biomass effectively stabilize the adsorbed metal ions as isolated SAs during the carbonization in Ar atmosphere. Characterizations by STEM, XANES, and EXAFS verify the atomic dispersion of Cu in the YHCs-Cu (0.01 mM). The optimized YHCs-Cu SAs anode exhibits well-developed graphitic domains, abundant nanopores, and regulated electronic structure, which collectively contribute to fast sodium-ion storage kinetics. As a result, it delivers a high ICE of 86.7% and outstanding long-term cycling stability: 95.3% capacity retention after 2500 cycles at 1C, and an ultralow capacity decay rate of 0.002% per cycle over 10,000 cycles at 5C. DFT calculations reveal that Cu SAs effectively lower the Na^+ diffusion barrier and enhance the electronic conductivity of the carbon matrix. Combined characterizations including Raman, XRD, GITT, and phenolphthalein-discoloration tests reveal a three-stage Na^+ storage mechanism: surface adsorption at high voltages, interlayer insertion at the early voltage plateau, and pore filling at the low-voltage plateau. Notably, this microbial approach can be extended to other transition metals (Fe, Ni, Co, Mn, Zn). All the as-prepared YHCs-SA samples exhibit high capacity retention (>96% after ~120 cycles), significantly superior to pristine YHCs. Moreover, YHCs-Cu SAs maintains robust

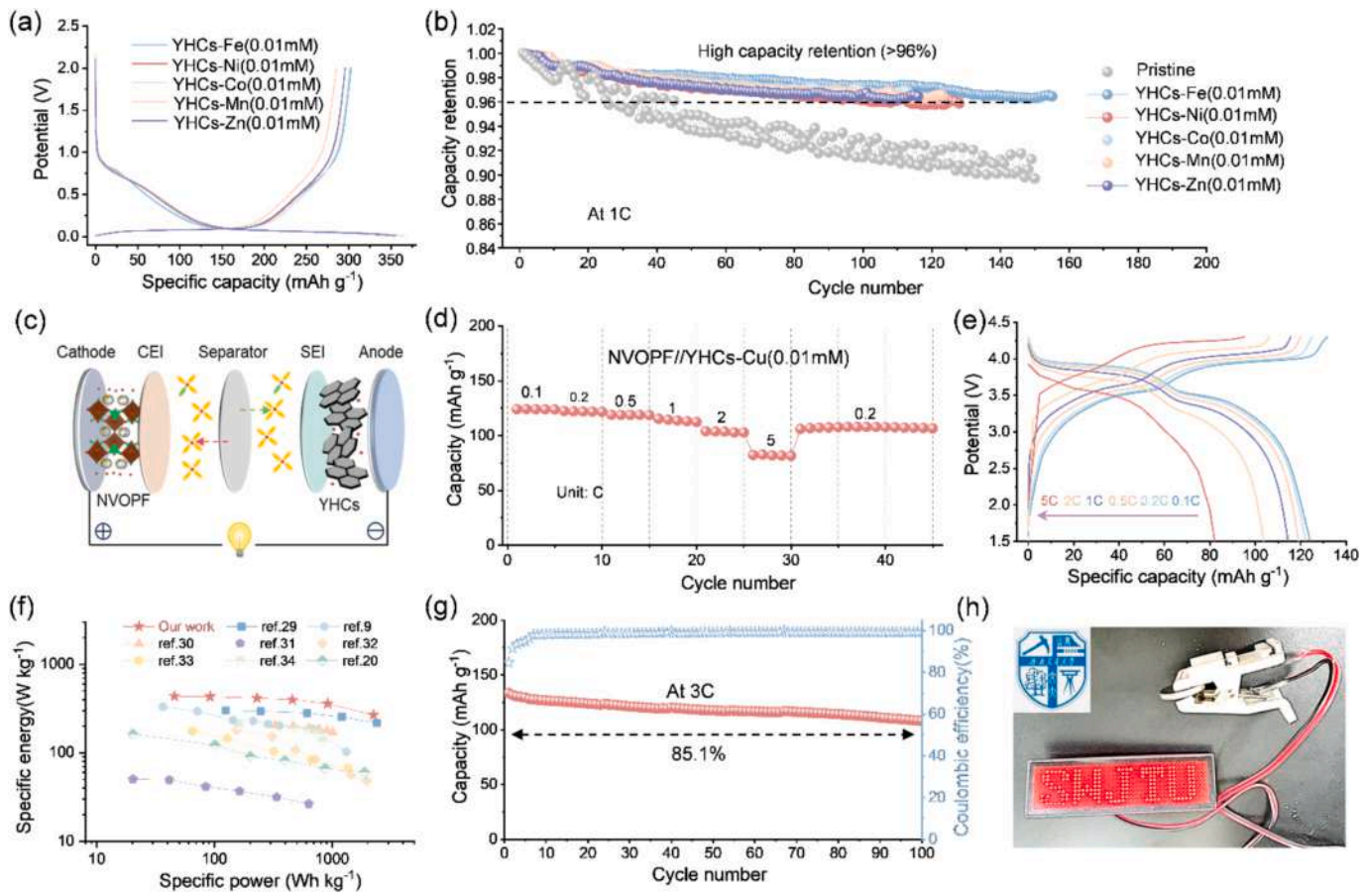


Fig. 6. (a) Discharge-charge curves of first cycle; (b) cycling performance of HCs with different metal single atoms; (c) schematic illustration of NVOPF//YHCs-Cu (0.01 mM) full cell; (d) rate performance; (e) charge–discharge curves; (f) YHCs-Cu(0.01 mM) electrode compared with previously HCs-based full cell: NHC-0.8 M-800 [35], Zn-HCs [14], a-C-NH [36], SRNDC-700 [37], HCNS [38], PCNS [39], HCM-1300 [40], HC-1400 [25]; (h) exhibition image of NVOPF//YHCs-Cu(0.01 mM) full cell during discharge.

electrochemical performance even at −20 °C in half-cells and achieves a high energy density of 323 Wh kg^{-1} in a full cell paired with an NVOPF cathode, demonstrating its practical feasibility. These findings highlight that biomass-directed synthesis offers a scalable, eco-friendly route for fabricating single-atom-modified carbon anodes, providing a promising strategy to boost the cycling stability of sodium-ion batteries.

Experimental section

Synthesis of YHCs without/with metals

Glucose was obtained from Aladdin Industrial Corporation and used without further purification. Yeast cells with high sugar tolerance were purchased from Taobao. Following a procedure adapted from our previous work, we first prepared an 80 mL aqueous glucose solution (0.2 M) in deionized water containing a defined concentration of Cu^{2+} (x = 0.001, 0.01, 0.1, or 1 mM). To this solution, 3.5 g of yeast cells were added, and the mixture was stirred at 30 °C for 24 h. To ensure efficient adsorption of Cu^{2+} onto yeast cells, the addition of Cu^{2+} was performed at the initial stage. The mixture was then transferred to a 100 mL autoclave and heated at 105 °C for 1 h to deactivate the yeast cells. After cooling to room temperature, the solid precursors were collected and washed twice each with deionized water and ethanol, followed by drying at 60 °C overnight. The dried precursors were placed in a graphite boat and calcined in a tubular furnace under an argon atmosphere. The temperature was raised from room temperature to 1300 °C at a heating rate of 3 °C min^{-1}, held at 1300 °C for 3 h, and then allowed to cool to 50 °C. The mass yield of the prepared hard carbons is approximately 12.3 wt% relative to the initial yeast cells. The resulting copper-containing, yeast-derived hard carbons were designated as YHCs-Cu(0.001 mM), YHCs-Cu(0.01 mM), YHCs-Cu(0.1 mM), and YHCs-Cu(1 mM). For comparison, a control sample (YHCs) was prepared following the same procedure but without the addition of Cu^{2+} to the initial glucose solution.

Synthesis of $Na_3V_2O_2(PO_4)_2F$ cathode

The $Na_3V_2O_2(PO_4)_2F$ cathode material was synthesized via a hydrothermal method adapted from previous publications. All reagents ($VOSO_4$, NaF, and NaH_2PO_4) with analytical purity, were sourced from Shanghai Aladdin Biochemical Technology Co., Ltd. In a typical synthesis, $VOSO_4$, NaF, and NaH_2PO_4 were combined in a molar ratio of 1: 1: 3 within a 100 mL Teflon-lined stainless-steel autoclave containing 40 mL of deionized water. The sealed autoclave was heated at 160 °C for 12 h, yielding a green precipitate. This product was collected, washed, and then dried under vacuum at 120 °C for 12 h to obtain the final $Na_3V_2O_2(PO_4)_2F$.

Material characterization

The morphologies of the synthesized HCs was examined using scanning electron microscopy (SEM, JSM 7800F Prime, Japan). Further structural details were analyzed by high-resolution transmission electron microscopy (HRTEM, JEOL JE-F200, Japan), revealing the crystalline arrangement of the HCs. X-ray diffraction (XRD, 18KW D/MAX2500V) was employed to assess the degree of graphitization.

Additionally, Raman spectroscopy (LabRAM HR Evolution, 532 nm excitation laser at 10% power) was used to evaluate the D and G bands of various YHCs samples. The specific surface area and pore structure of the HCs were determined through nitrogen adsorption–desorption measurements (ASAP 2460, Micromeritics, USA). X-ray photoelectron spectroscopy (XPS, Thermo Scientific K-Alpha) provided insights into the elemental composition and chemical states. high-angle annular darkfield scanning transmission electron microscope (HAADF-STEM) images were recorded on a Titan Cubed Themis G2 300. Cu K-edge extended X-ray absorption fine structure data were collected at the Australian Synchrotron.

Electrochemical measurement

HCs anodes were fabricated using a standard slurry-coating process. A slurry was prepared by mixing the HC active material, Super P conductive carbon, and sodium alginate binder in an 8:1:1 wt ratio with deionized water. This slurry was uniformly coated onto copper foil, dried at 60 °C for 6 h, and then vacuum-dried at 100 °C for 12 h. The electrodes were subsequently punched into 10 mm disks, preparing an active material loading of 1.2–1.5 mg cm^{-2}. CR2032 coin-type half-cells were assembled in an argon-filled glove box (O_2 < 0.01 ppm, H_2O < 0.01 ppm) using the HC electrode as the working electrode, sodium metal as the counter electrode, a glass fiber separator (Whatman GF/A), and 1 M $NaPF_6$ in diglyme as the electrolyte. For full-cell evaluations, pre-sodiated HC anodes were coupled with $Na_3V_2O_2(PO_4)_2F$ cathode with negative/positive ratio of ~1.2, using 1 M $NaClO_4$ in EC: DEC (1:1 v/v) as the electrolyte and a voltage window of 1.5–4.3 V. Electrochemical characterization was performed as follows: Cyclic voltammetry (CV) at 0.1–1.0 mV s^{-1} (CHI660E workstation), galvanostatic charge/discharge (GCD) between 0.01 and 2.0 V *vs.* Na^+/Na (NEWARE tester, 25 °C and −20 °C), electrochemical impedance spectroscopy (EIS) from 100 kHz to 0.1 Hz, and galvanostatic intermittent titration technique (GITT) with a 30 mA g^{-1} current pulse (10 min on, 60 min rest) to determine the Na^+ diffusion coefficient.

Density Functional Theory (DFT) calculation

In this study, all first-principles calculations in this paper were performed using the Vienna ab-initio simulation package (VASP). The Projector Augmented Wave (PAW) method was used as the basis functions to describe the interactions between electrons and ions. Under the Generalized Gradient Approximation (GGA), the Perdew-Burke-Ernzerhof (PBE) functional was employed to handle the exchange–correlation effects of electrons, and the DFT-D3 was used to correct the van der Waals interactions. During the relaxation process, the interruption criterion for the electronic self-consistent cycle is set to 10^{-5} eV, the maximum force on each atom was limited to 0.02 eV/Å, and the cutoff energy for the plane wave basis set was set to 600 eV. The energy potential of W ion migration was calculated by using the climbing image nudged elastic band (CINEB) method.

Self-assembled in-situ Raman instrument

We designed an instrument for the *in-situ* Raman measurement using optical quartz glass to transmit the laser and collect the scattered Raman signals. Specifically, we created a 3 mm hole in the cathodic case and affixed the quartz glass to it. To allow the laser to directly irradiated on HCs anode, we employed copper screen as current collector. The designed Raman instrument was assembled in an argon-filled glove box. During the discharge–charge process, the coin battery was positioned on a Raman instrument, with a 532 nm laser providing continuous irradiation.

Author contributions

The manuscript was written through contributions of all authors. All authors have given approval to the final version of the manuscript.

CRediT authorship contribution statement

Guilin Feng: Writing – original draft, Methodology, Investigation, Formal analysis, Conceptualization. **Xiaohong Liu:** Formal analysis, Data curation. **Xiaoming Tu:** Writing – review & editing, Formal analysis. **Wen Xi:** . **Hanying Wang:** Software, Data curation. **Lei Zhou:** Software, Data curation. **Chen Wu:** Writing – review & editing, Software. **Panpan Dong:** Writing – review & editing. **Chunliu Xu:** Writing – review & editing, Formal analysis. **Weiqing Yang:** Writing – review & editing, Supervision.

Declaration of competing interest

The authors declare that they have no known competing financial interests or personal relationships that could have appeared to influence the work reported in this paper.

Acknowledgements

This work was supported by National Natural Science Foundation of China (No. 52372228, No. 22309203, No. 22508025), the Sichuan Science and Technology Program (No. 2026NSFSC0896, No. 2025ZNSFSC0364, No. 2025ZNSFSC0967), and China Postdoctoral Science Foundation (2024M752669, 2024M762671). Dr. X. Liu thanks financial support from "Research start-up Fund" of Chengdu University of Technology (No. 10912-KYQD2024-10455). Dr. G. Feng and Dr. C. Xu acknowledge financial support from the Fundamental Research Funds for the Central Universities (Grant Number: 2682025CX003, 2682025CX145). We thank the Analysis and Testing center of Southwest Jiaotong University and Scientific Compass (*www.shiyanjia.com*) for allowing us to use SEM, TEM, XRD, and BET. We thank eceshi (*www.eceshi.com*) for the DFT calculation.

Appendix A. Supplementary data

Supplementary data to this article can be found online at https://doi.org/10.1016/j.mattod.2026.103296.

Data availability

Data will be made available on request.

References

[1] Y. Zhang, et al., Nat. Commun. 16 (2025) 3634.
[2] E. Dogan, et al., J. Power Sources 668 (2026) 239365.
[3] E. Dogan, et al., Adv. Sustain. Syst. (2025) e01668.
[4] S. Xiao, et al., Adv. Mater. 37 (2025) 2501434.
[5] Z.-M. Oktay, et al., J. Mater. Sci. Mater. Electron. 34 (2023) 1543.
[6] H. Zhang, et al., Mater. Today 85 (2025) 231–252.
[7] R. Whba, et al., Ionics 31 (2025) 1537–1554.
[8] Y. He, et al., Adv. Funct. Mater. 34 (2024) 2403144.
[9] Z.-G. Liu, et al., Chem. Sci. 15 (2024) 8478.
[10] C. Yang, et al., Carbon Energy 6 (2024) e503.
[11] T.H. Hong, et al., Mater. Today 89 (2025) 57–66.
[12] X. Ma, et al., Adv. Funct. Mater. (2025).
[13] C. Xue, et al., Energy Mater. 5 (2025) 500113.
[14] Z. Lu, et al., Adv. Mater. 35 (2023).
[15] D. Qiu, et al., Adv. Energy Mater. (2024).
[16] B. Pei, et al., Sci. Bull. 70 (2025) 2104–2115.
[17] K. Liu, et al., Nat. Commun. 16 (2025) 1203.
[18] J. Zhao, et al., Adv. Funct. Mater. (2025) e21090.
[19] S. Zhang, et al., ACS Nano 19 (2025) 26892–26903.
[20] G. Feng, et al., Energy Storage Mater. (2025) 104559.
[21] G. Zhang, et al., Angew. Chem. Int. Ed. 64 (2025).
[22] S. Wu, et al., Adv. Funct. Mater. 35 (2025).

[23] Y. Qiu, et al., Adv. Funct. Mater. (2025).
[24] S. You, et al., Energy Environ. Sci. 17 (2024) 8189.
[25] Z. Tang, et al., Nat. Commun. 14 (2023) 6024.
[26] M.-Y. Su et al., 43 (2024) 2585–2596.
[27] M. Li, et al., Green Chem. 27 (2025) 2696–2705.
[28] G. Feng, et al., Nano Energy 136 (2025) 110728.
[29] Z. Huang, et al., J. Am. Chem. Soc. 147 (2025) 45763–45773.
[30] G. Feng, et al., Nanoscale 15 (2023) 4932–4939.
[31] J. Wang, et al., Adv. Funct. Mater. 34 (2024).
[32] X. Feng, et al., Energy Environ. Sci. 17 (2024) 1387–1396.
[33] C..Y Wu, et al., Angew. Chem. Int. Ed. 63 (2024).
[34] C. Xu, et al., ACS Nano 18 (2024) 18758–18768.
[35] Y.-J. Xu, et al., Energy Storage Mater. 75 (2025) 104031.
[36] P. Wang, et al., ACS Nano 19 (2025) 38735–38748.
[37] B. Yin, et al., Adv. Mater. 33 (2021).
[38] R. Dong, et al., Adv. Mater. 33 (2021).
[39] M. Hao, et al., Fuel Process. Technol. 177 (2018) 328.
[40] X. Yin, et al., Adv. Mater. 34 (2022).